Research Square

Preprints are preliminary reports that have not undergone peer review.
They should not be considered conclusive, used to inform clinical practice,
or referenced by the media as validated information.

Integrated Spectral-Habitat Imaging with Explainable Artificial Intelligence for Preoperative Prediction of Perineural Invasion in Gastric Adenocarcinoma

Chong Wang
the Affiliated Hospital of Xuzhou Medical University
Zhen Wang
the Affiliated Hospital of Xuzhou Medical University
Xiaohan Liu
the Affiliated Hospital of Xuzhou Medical University
Chen Wu
the Affiliated Hospital of Xuzhou Medical University
Xiaolong Wang
the Affiliated Hospital of Xuzhou Medical University
Shang Jin
the Affiliated Hospital of Xuzhou Medical University
He Zhang
the Affiliated Hospital of Xuzhou Medical University
Yixin Xu
the Affiliated Hospital of Xuzhou Medical University
Aiyun Sun
GE HealthCare
Tao Ding
the Affiliated Hospital of Xuzhou Medical University
Kai Xu
the Affiliated Hospital of Xuzhou Medical University
Yankai Meng
mengyankai@126.com

the Affiliated Hospital of Xuzhou Medical University

Research Article

Keywords:

Posted Date: May 19th, 2026

DOI: https://doi.org/10.21203/rs.3.rs-9632157/v1

License: This work is licensed under a Creative Commons Attribution 4.0 International License.
Read Full License

Additional Declarations: No competing interests reported.

Version of Record: A version of this preprint was published at Abdominal Radiology on July 13th, 2026.
See the published version at https://doi.org/10.1007/s00261-026-05677-w.

Abstract

Background

Perineural invasion (PNI) is a key prognostic determinant in gastric adenocarcinoma but remains radiologically occult on conventional CT.

Purpose

To develop and validate an integrated model combining dual-energy CT (DECT)–derived functional spectral slopes and subregional habitat signatures for the preoperative prediction of PNI.

Materials and Methods

In this retrospective study, 175 patients (median age, 67 years; 131 men) with gastric adenocarcinoma who underwent preoperative DECT between 2023 and 2025 were evaluated. Patients were randomized into a training cohort (*n* = 122) and an independent test cohort (*n* = 53). Tumor subregions were parcellated into three biologically distinct habitats using voxel-wise clustering. Stable habitat features (ICC ≥ .75) and three-phase spectral slopes were integrated using a combined model. Diagnostic performance was evaluated using the area under the receiver operating characteristic curve (AUC). Clinical utility was assessed via decision curve analysis.

Results

PNI was pathologically confirmed in 46.9% (82 of 175) of patients. The integrated Spectral-Habitat model achieved an AUC of .748 (95% CI: .654, .837) in the training cohort and .753 (95% CI: .608, .881) in the independent test cohort. The combined model significantly outperformed the habitat-radiomics baseline (AUC, .753 vs .607; *P* = .011). Equilibrium-phase spectral slope emerged as the most decisive functional biomarker. Model calibration was excellent in the test cohort (*P* = .560, Hosmer-Lemeshow test). Decision curve analysis demonstrated a substantial net clinical benefit across threshold probabilities of 10%–80%.

Conclusion

An integrated model leveraging functional spectral kinetics and subregional spatial heterogeneity improves the preoperative prediction of occult perineural invasion, providing a potential tool for personalized surgical decision-making.

Introduction

Gastric adenocarcinoma is characterized by profound biological heterogeneity and remains a leading cause of cancer-related mortality worldwide (1, 2). Among various histopathological markers, perineural invasion (PNI)—the neoplastic invasion of tumor cells into the neural sheath—is established as a robust independent predictor of local recurrence and poor overall survival (3, 4). Preoperative identification of PNI is clinically pivotal, as its presence may necessitate more extensive neural plexus clearance (e.g., celiac or superior mesenteric plexus dissection) and facilitate the selection of candidates for aggressive neoadjuvant therapy (5, 6). However, PNI is a microscopic infiltrative process that remains radiologically occult on conventional macroscopic CT, and current preoperative staging systems lack reliable non-invasive biomarkers to predict its presence (7).

Dual-energy CT (DECT) has emerged as a functional imaging modality capable of quantifying the tumor microenvironment (TME) beyond simple Hounsfield units (8). While parameters such as iodine concentration and extracellular volume (ECV) fraction have shown promise in assessing tumor desmoplasia, these conventional macroscopic metrics typically rely on whole-tumor averaging (9, 10). This global approach inherently dilutes focal aggressive signals and masks the subtle spatial heterogeneity of the tumor-nerve interface(11). Subregional habitat imaging, which employs voxel-wise clustering to parcellate the tumor into biologically distinct niches, offers a potential solution by isolating specific stromal and infiltrative subregions associated with neuro-invasion (12, 13).

Beyond iodine quantification, the spectral slope (λHU)—derived from the energy-dependent attenuation decay curve—provides a more granular reflection of iodine kinetics and interstitial fluid pressure (13). Pathophysiologically, the tumor-nerve interface is now recognized as a specialized "neural niche" where dense desmoplastic remodeling and altered microvascular permeability occur (14). Recent evidence even suggests intense metabolic crosstalk at this interface, including mitochondrial transfer from neurons to cancer cells which enhances metastatic plasticity (13). This unique pathophysiology significantly impacts the dynamic washout characteristics of iodinated contrast, particularly during the equilibrium phase. Despite the potential synergy between functional spectral decay kinetics and spatial habitat phenotypes, their combined diagnostic value for PNI prediction remains unexplored.

Furthermore, traditional machine learning models often treat subregions as independent variables, failing to capture the structural organization of the TME. Graph neural networks (GNNs) enable the modeling of high-order spatial interactions and topological relationships between tumor habitats (15–17). By integrating functional spectral parameters with GNN-derived spatial signatures supported by explainable artificial intelligence (XAI), we may achieve a more comprehensive and transparent decoding of the radiologically occult PNI phenotype (18).

Therefore, the purpose of this study was to develop and validate an integrated model combining DECT-derived three-phase spectral slopes and subregional habitat spatial signatures for the preoperative prediction of PNI in patients with gastric adenocarcinoma. We hypothesized that this multi-modal approach, supported by topological interaction modeling, would provide superior diagnostic efficacy and clinical utility compared with conventional global imaging metrics.

Materials and Methods

Patient Population

This retrospective, single-center study was approved by the Institutional Review Board, and the requirement for written informed consent was waived. Between November 2023 and May 2025, 473 consecutive patients with pathologically confirmed gastric adenocarcinoma who underwent preoperative three-phase DECT were screened. The inclusion criteria were: (a) surgical resection with curative intent; (b) complete histopathologic evaluation of PNI status; and (c) high-quality DECT images. Patients were excluded if they: (a) received neoadjuvant therapy (*n* = 164); (b) lacked complete clinicopathological data (*n* = 89); (c) had specific histological subtypes (*n* = 28); (d) had other malignancies (*n* = 14); or (e) showed poor image quality (*n* = 3). The final cohort (*n* = 175) was randomly partitioned into a training cohort (*n* = 122) and an independent test cohort (*n* = 53) using a stratified 7:3 ratio.

DECT Image Acquisition and Spectral Parameters

All examinations were performed using one of two dual-energy CT scanners: a third-generation dual-source CT scanner (SOMATOM Force; Siemens Healthineers, Erlangen, Germany) or a rapid kVp-switching spectral CT scanner (Revolution CT; GE HealthCare, Waukesha, Wis). For the Siemens scanner, the DECT protocol utilized 90/Sn150 kVp. For the GE scanner, images were acquired using the Gemstone Spectral Imaging (GSI) mode with rapid switching between 80 kVp and 140 kVp. Regardless of the scanner used, a standard three-phase DECT protocol (arterial, venous, and 3-minute delayed equilibrium phases) was uniformly applied.

A nonionic iodinated contrast material (Ioversol, 350 mg I/mL, Optiray 350; Guerbet, Villepinte, France) was administered intravenously via a power injector at a weight-based dose of 1.2 mL/kg and a flow rate of 2.5–3.5 mL/sec, followed by a 40-mL saline flush.

To minimize multi-vendor variability and ensure the stability of high-order texture features across the Siemens and GE platforms, all images were reconstructed using a standardized slice thickness of 1.25 mm with a standard soft-tissue kernel. This thin-section reconstruction protocol was adopted to comply with the International Biomarker Standardization Initiative (IBSI) recommendations, aiming to preserve spatial resolution and reduce partial volume effects in the subregional habitat analysis.

Tumor Segmentation and Volumetric Analysis

Two abdominal radiologists (with 6 and 13 years of experience, respectively), blinded to the clinicopathologic results, independently performed the image analysis. Post-processing and the generation of quantitative iodine maps were performed on vendor-specific workstations (syngo.via for Siemens and AW VolumeShare for GE).

Two abdominal radiologists (with 6 and 13 years of experience, respectively), blinded to the clinicopathologic results, independently performed the image analysis. Whole-tumor volumetric regions of interest (VOIs) were manually delineated on all contiguous axial slices along the contour of the solid tumor portion using 3D Slicer (version 5.6.2; www.slicer.org). To ensure boundary precision, segmentations were primarily performed on venous-phase iodine maps, which provide optimal contrast between the tumor and the surrounding gastric wall. Delineation strictly avoided peritumoral edema, intraluminal gas, cystic necrosis, and macroscopic peritumoral blood vessels.

To quantify functional kinetics (Innovation B), the 3D mean spectral slope (λ_{HU}) was calculated from the entire tumor volume for each phase using the formula: $\lambda=(HU_{40keV}-HU_{70keV})/30$.

3D Habitat Delineation and Feature Extraction

To capture spatial heterogeneity (Innovation C), an unsupervised 3D voxel-wise habitat phenotyping pipeline was implemented. The K-means clustering algorithm (k = 3) was applied to all voxels within the 3D tumor VOI, parcellating the volume into three biologically distinct niches: Habitat 1 (hypervascular core), Habitat 2 (transition zone), and Habitat 3 (necrotic/desmoplastic stroma)(12). A 3D spatial median filter (3×3×3 voxel kernel) was applied to the clustered maps to ensure biological contiguity and eliminate noise. High-throughput radiomic features were then extracted from each 3D habitat subregion in compliance with the International Biomarker Standardization Initiative (IBSI) guidelines.

Feature Selection and Model Construction

High-throughput features were extracted from the three habitats using the IBSI-compliant PyRadiomics library. Inter-observer reproducibility was assessed via intraclass correlation coefficients (ICCs), and only stable features (ICC ≥ .75) were retained. Dimensionality reduction was achieved through redundancy filtering ($|\rho| > .90$) and LASSO regression with 10-fold cross-validation.

To decode high-order spatial interactions, a Habitat-Graph Neural Network (H-GNN) architecture was employed. The H-GNN modeled the spatial adjacency of the three habitats as edges, extracting topological signatures that were then integrated with the functional spectral slopes using a robust Logistic Regression framework to generate the final Spectral-Habitat Signature (Rad-score).

The final Spectral-Habitat Signature (Rad-score) was calculated for each patient as a linear combination of the selected features weighted by their respective standardized LASSO coefficients as follows:

Rad-score =

.1183 × *hab1_RootMeanSquared*

+ .0994 × *Slope_EP*

+ .0686 × *hab2_LargeAreaLowGrayLevelEmphasis*

+ .0209 × *hab1_RunVariance*

+ .0181 × *hab3_SmallDependenceHighGrayLevelEmphasis*

+ .0112 × *hab1_DependenceVariance*

+ .0101 × *Slope_VP*

+ .0067 × *hab3_DifferenceEntropy*

+ .0022 × *hab1_90Percentile*

+ .0007 × *hab2_LargeAreaHighGrayLevelEmphasis*

- **– .0116** × *hab2_DifferenceVariance*
- **– .0434** × *hab3_SmallAreaLowGrayLevelEmphasis*

Note

— All radiomic and spectral features used in the formula were z-score standardized based on the mean and standard deviation of the training cohort. EP = equilibrium phase, Hab = subregional habitat, VP = venous phase.

Statistical Analysis

The primary endpoint was pathologically confirmed PNI. Diagnostic performance was evaluated using AUC with 95% CIs. Model comparison was performed via the DeLong test. Calibration and clinical utility were assessed using the Hosmer-Lemeshow test, Brier scores, and decision curve analysis (DCA). Spearman correlation associated imaging features with pathological aggressiveness. All tests were two-sided; $P < .05$ indicated statistical significance.

Results

Patient Characteristics and Cohort Partitioning

Between November 2023 and May 2025, a total of 473 consecutive patients diagnosed with gastric adenocarcinoma were screened. After the application of exclusion criteria (Fig. 1), 175 patients (median age, 67 years; IQR, 58–73; 131 men) were finally enrolled for the PNI analysis.

The study population was randomly partitioned into a training cohort ($n = 122$) and an independent test cohort ($n = 53$). Perineural invasion was pathologically confirmed in 46.7% (57 of 122) of patients in the training cohort and 47.2% (25 of 53) of patients in the independent test cohort ($P > .99$). As shown in Table 1, there were no significant differences in demographic characteristics, pT stage, or quantitative DECT parameters between the two cohorts (all $P > .05$).

Table 1
Baseline Clinical, Pathological, and Quantitative DECT Characteristics of the Training and Test Cohorts

Characteristic	Overall (*n* = 175)	Training Cohort (*n* = 122)	Independent Test Cohort (*n* = 53)	*P* Value
Gender (Male)	131 (74.9)	87 (71.3)	44 (83.0)	.147
Pathological Findings				
PNI Positive	82 (46.9)	57 (46.7)	25 (47.2)	1.000
Advanced Stage (pT3–4)	125 (71.4)	87 (71.3)	38 (71.7)	.803
Invasion Status (Positive)	112 (64.0)	79 (64.8)	33 (62.3)	.886
DECT Parameters				
Slope_AP *	2.2 [1.5, 2.9]	2.2 [1.3, 3.0]	2.1 [1.6, 2.8]	.964
Slope_VP *	3.1 [2.3, 3.7]	3.0 [2.2, 3.6]	3.2 [2.4, 3.9]	.176
Slope_EP *	2.7 [2.1, 3.3]	2.7 [2.1, 3.3]	2.9 [2.2, 3.4]	.665
ECV (%) †	0.4 ± 0.1	0.4 ± 0.1	0.4 ± 0.1	.164

Note.— Data in parentheses are percentages. AP = arterial phase, DECT = dual-energy CT, ECV = extracellular volume fraction, EP = equilibrium phase, PNI = perineural invasion, VP = venous phase.

* Data are medians, with interquartile ranges in parentheses.

† Data are means ± standard deviations.

Inter-observer Reproducibility and Feature Selection

Stability and Reproducibility

Inter-observer agreement for the quantitative DECT parameters and subregional habitat features was highly robust. As shown in **Figure E1** and Table 2, all 19 quantitative DECT parameters and 10 selected radiomic features exceeded the pre-specified stability threshold (ICC ≥ .75). Specifically, the functional spectral slopes showed exceptional stability: the venous phase slope (Slope_VP) yielded an ICC of .914, while the arterial (Slope_AP) and equilibrium phase (Slope_EP) slopes yielded ICCs of .863 and .833, respectively. The global ECV fraction also demonstrated substantial agreement (ICC, .760).

Feature Selection and Signature Construction

In the training cohort (*n* = 122), a total of 264 stable habitat features (88 from each of the three subregional habitats) along with the quantitative spectral parameters were subjected to LASSO

regression with 10-fold cross-validation. Through this dimensionality reduction pipeline, 12 robust predictors with non-zero coefficients were identified to construct the final Spectral-Habitat Signature (**Figure E2**). These predictors comprised two functional spectral parameters (Slope_EP and Slope_VP) and ten subregional habitat radiomic features distributed across the hypervascular core (Habitat 1, *n* = 4), transition zone (Habitat 2, *n* = 3), and necrotic stroma (Habitat 3, *n* = 3). The intensity-based feature from Habitat 1 (RootMeanSquared) and the functional kinetic parameter (Slope_EP) emerged as the most decisive positive predictors, with standardized coefficients of .1183 and .0994, respectively (Table 2).

Table 2
Constituent Features of the Spectral-Habitat Signature and Their Reproducibility

Feature Source	Radiomic or Spectral Feature	Feature Category	ICC (95% CI)	LASSO Coefficient
Spectral	Slope_EP	Functional Kinetic	.833 [.752, .894]	.0994
	Slope_VP	Functional Kinetic	.914 [.850, .960]	.0101
Habitat 1	RootMeanSquared	First-order	.921 [.865, .960]	.1183
	RunVariance	GLRLM (Texture)	.892 [.810, .942]	.0209
	DependenceVariance	GLDM (Texture)	.910 [.842, .951]	.0112
	90thPercentile	First-order	.945 [.890, .975]	.0022
Habitat 2	LargeAreaLowGrayLevelEmphasis	GLSZM (Texture)	.860 [.785, .921]	.0686
	LargeAreaHighGrayLevelEmphasis	GLSZM (Texture)	.881 [.810, .935]	.0007
	DifferenceVariance	GLCM (Texture)	.842 [.751, .903]	–.0116
Habitat 3	SmallDependenceHighGrayLevelEmphasis	GLDM (Texture)	.885 [.802, .934]	.0181
	DifferenceEntropy	GLCM (Texture)	.890 [.815, .940]	.0067
	SmallAreaLowGrayLevelEmphasis	GLSZM (Texture)	.874 [.791, .928]	–.0434

Note.— Data in brackets are 95% CIs. CI = confidence interval, EP = equilibrium phase, GLCM = gray-level co-occurrence matrix, GLDM = gray-level dependence matrix, GLRLM = gray-level run length matrix, GLSZM = gray-level size zone matrix, ICC = intraclass correlation coefficient, VP = venous phase.

Diagnostic Performance and Validation of the Integrated Model

Distribution of the Spectral-Habitat Signature

The Spectral-Habitat Rad-score exhibited a significantly different distribution between PNI-positive and PNI-negative patients. In the training cohort (*n* = 122), PNI-positive patients showed a markedly higher median Rad-score compared to PNI-negative patients (median, .12 [IQR: .01, .24] vs −.10 [IQR: −.25, .01]; *P* < .001, Fig. 2A). This discriminatory power was successfully validated in the independent test cohort (*n* = 53), where PNI-positive patients maintained significantly elevated scores (median, .05 [IQR: −.09, .25] vs −.11 [IQR: −.21, .07]; *P* = .047, Fig. 2B).

Diagnostic Efficacy and Model Validation

The integrated Spectral-Habitat model achieved consistent diagnostic performance across both cohorts. In the training cohort (*n* = 122), the signature yielded an AUC of .748 (95% CI: .654, .837). The performance was robustly generalized to the independent test cohort (*n* = 53), which showed a validated AUC of .753 (95% CI: .608, .881) (Fig. 3 and Table 3). These results demonstrate the high stability of the multi-modal signature in differentiating PNI-positive from PNI-negative gastric cancer.

Table 3
Diagnostic Performance of the Integrated Spectral-Habitat Signature for Predicting Perineural Invasion

Metric	Training Cohort (*n* = 122)	Independent Test Cohort (*n* = 53)
AUC	.748 (.654, .837)	.753 (.608, .881)
Sensitivity (%)	64.9 (37/57) [.518, .765]	68.0 (17/25) [.500, .857]
Specificity (%)	81.5 (53/65) [.720, .898]	71.4 (20/28) [.550, .871]
Accuracy (%)	73.8 (90/122) [.664, .811]	69.8 (37/53) [.585, .811]
PPV (%)	75.5 (37/49) [.628, .864]	68.0 (17/25) [.500, .850]
NPV (%)	72.6 (53/73) [.616, .819]	71.4 (20/28) [.542, .879]

Note.— Data in parentheses are 95% CIs calculated using 1000 bootstrap iterations. Data in brackets are the raw numbers used to calculate percentages. The optimal threshold for all metrics was determined by the Youden index in the training cohort and subsequently applied to the independent test cohort.

AUC = area under the receiver operating characteristic curve, NPV = negative predictive value, PNI = perineural invasion, PPV = positive predictive value.

Note

— Dual-violin and box plots illustrate the scores for patients with (red) and without (blue) pathologically confirmed perineural invasion (PNI) in the **(A)** training cohort (*n* = 122) and **(B)** independent test cohort (*n* = 53). Horizontal lines within the boxes indicate medians; boxes indicate the interquartile range; and whiskers indicate the range of data excluding outliers. Shaded areas represent the kernel density estimation of the score distribution. Individual data points are shown as jittered dots. *P* values were derived from the Mann-Whitney U test. The discriminatory power of the signature was successfully validated in the independent test cohort (**P = .047**).

Note

— Curves illustrate the diagnostic performance of the integrated model in the **(A)** training cohort and **(B)** independent test cohort. The training cohort yields an AUC of .748 (95% CI: .654, .837), and the independent test cohort yields a validated AUC of .753 (95% CI: .608, .881). The proximity of the AUC values between cohorts indicates excellent model generalizability and a lack of overfitting. The integrated model (red solid line) demonstrated significantly improved performance compared with the habitat-only radiomics baseline (blue dashed line) in the test set (*P*=.011, DeLong test).

Clinical Utility, Calibration, and Individualized Risk Estimation

Clinical Utility and Biological Correlation

To further elucidate the biological basis of the signature, Spearman correlation analysis was performed (**Figure E3**). Functional spectral kinetic parameters exhibited strong associations with microscopic tumor aggressiveness, providing a link between macroscopic energy-spectrum kinetics and subregional spatial heterogeneity.

Supplementary Figure E3: Biological correlation between the Habitat-Spectral signature and pathological markers.

Note

— Heatmap illustrates Spearman correlation coefficients (ρ) between the three components of the integrated model and macroscopic pathological findings. Venous-phase spectral slope (Slope_VP) shows the strongest negative association with invasion status ($r = -.48$, $P < .001$), supporting its role as a functional surrogate for tissue microenvironment remodeling.

Model Calibration and Reliability

The integrated Spectral-Habitat model demonstrated excellent calibration in both the training and independent test cohorts (Fig. 4A). The Brier scores were .202 for the training cohort and .203 for the independent test cohort, indicating high predictive accuracy. Furthermore, the Hosmer-Lemeshow test

yielded non-significant results for both the training (*P* = .882) and test (*P* = .560) cohorts, confirming that there was no significant discrepancy between the model-predicted probabilities and the actual observed frequency of PNI.

Clinical Benefit and Individualized Scoring

Decision curve analysis substantiated the clinical actionable value of the proposed signature (Fig. 4B). In the independent test set, the integrated model provided a higher net clinical benefit than the 'treat-all' and 'treat-none' strategies across a wide range of threshold probabilities (10%–80%).

To facilitate personalized surgical decision-making, we quantified the feature-level contribution to the final risk score (Fig. 4C). Functional spectral kinetics were the primary drivers of the model's weight system. Specifically, the equilibrium-phase spectral slope (Slope_EP) emerged as the most decisive functional biomarker (assigned 100 points in the scoring system), followed by the venous-phase spectral slope (Slope_VP), underscoring the vital role of functional iodine kinetics in decoding the perineural microenvironment.

Discussion

In this study, we developed and validated an integrated model combining functional DECT spectral slopes and subregional habitat signatures for the preoperative prediction of PNI in gastric adenocarcinoma. Our integrated model achieved a robust and consistent diagnostic performance, with an AUC of .748 in the training cohort and a validated AUC of .753 in the independent test cohort. Notably, the multi-modal signature provided a significant performance leap over the habitat-radiomics baseline (*P* = .011), and the equilibrium-phase spectral slope (Slope_EP) emerged as the most decisive functional biomarker. These findings suggest that the synergy of functional iodine kinetics and spatial heterogeneity analysis effectively decodes the radiologically occult phenotype of PNI.

The biological plausibility of our model centers on the synergy between functional iodine kinetics and subregional spatial heterogeneity. In our study, the equilibrium-phase spectral slope (λ_{HU}) emerged as the most decisive biomarker, contributing the maximum weight in the point-based risk score. This likely reflects the altered microvascular permeability and dense desmoplastic remodeling characteristic of the "neural niche"(19). Pathophysiologically, the tumor-nerve interface is a site of intense metabolic crosstalk, including mitochondrial transfer from neurons to cancer cells, which enhances metastatic plasticity(13). These complex biological alterations, coupled with increased interstitial fluid pressure, result in sluggish iodine washout kinetics, providing a mechanistic basis for the superior predictive value of delayed-phase spectral parameters over conventional macroscopic metrics like ECV.

Furthermore, our targeted habitat imaging approach overcomes the critical limitation of signal dilution inherent in whole-tumor averaging. By parcellating the tumor into biologically distinct niches, we identified that spatial heterogeneity features from Habitat 3 (necrotic/desmoplastic stroma) were indispensable for PNI prediction. As illustrated in our representative cases, PNI-positive tumors characteristically exhibited a fragmented and infiltrative distribution of this stromal habitat. This "spatial

chaos" likely reflects high-order micro-architectural heterogeneity and the expansion of aggressive cell clones interacting with the perineural environment(20, 21).

Our findings further validate the clinical utility of subregional analysis in gastric adenocarcinoma, echoing recent large-scale evidence where a three-subregion habitat model successfully decoded HER2 status by capturing similar micro-architectural nuances(12). The superior performance of our integrated model over the habitat-only baseline suggests that functional DECT kinetics provide the essential "biological signal," while subregional spatial phenotypes provide the necessary "anatomical context" to accurately predict the radiologically occult phenotype of perineural invasion.

The clinical utility of our signature is substantiated by the decision curve analysis, which demonstrated a substantial net clinical benefit across a wide threshold range (10%–80%). Preoperative identification of PNI is a long-standing surgical challenge, as it is often undetected even by experienced radiologists on conventional CT(22). Our model provides a non-invasive tool to bridge this gap. For patients identified as high-risk by the Spectral-Habitat signature, surgeons may consider escalating the extent of lymphadenectomy or performing more meticulous celiac and superior mesenteric plexus clearance, moving the field toward "virtual pathological mapping" and personalized surgical oncology.

Our study has several limitations. First, this was a retrospective, single-center study. Although a rigorous 7:3 independent validation was performed, multi-institutional and multi-vendor external cohorts are required to confirm the cross-platform generalizability of our Habitat-Spectral signature. Second, while 3D volumetric analysis was employed to capture the full spatial dynamics of the tumor, manual segmentations are inherently labor-intensive and subject to inter-reader variability, especially in delineating the subtle gastric wall-serosa interface. Finally, while we utilized explainable AI to demystify the model, the complex interactions within the GNN architecture require further "glass-box" refinement for clinical transparency.

Conclusion

In conclusion, an integrated model leveraging functional DECT spectral slopes and subregional habitat signatures provides a robust, non-invasive method for the preoperative prediction of PNI in gastric adenocarcinoma. This approach successfully bridges the gap between macroscopic imaging and microscopic pathology, offering a promising tool for individualized surgical decision-making.

Abbreviations

AUC
area under the receiver operating characteristic curve
CI
confidence interval
DECT
dual-energy CT

DCA
decision curve analysis
ECV
extracellular volume fraction
EP
equilibrium phase
ICC
intraclass correlation coefficient
LASSO
least absolute shrinkage and selection operator
PNI
perineural invasion
ROI
region of interest
VP
venous phase

Declarations

Competing interests:

The authors have no competing interests to declare that are relevant to the content of this article.

Ethical approval:

This retrospective, single-center study was approved by the Institutional Review Board, and the requirement for written informed consent was waived.

Author Contribution

C W: Conceptualization, study design, data curation, data analysis, writing original draftZ W: Conceptualization, study design, data curation, data analysis, writing original draftXH L:Conceptualization, study design, data curation, data analysis, writing original draftC W, XL W, H Z,T D,YX X,K X,S J,: Diagnostic validationAiyun Sun: Conceptualization, supervisionYankai Meng: Conceptualization, study design, data analysis, writing review and editing

Data Availability Statement:

The datasets generated and/or analyzed during the current study are not publicly available due to patient privacy protection but are available from the corresponding author on reasonable request.

References

1. Sung H, Ferlay J, Siegel RL, Laversanne M, Soerjomataram I, Jemal A, Bray F. Global Cancer Statistics 2020: GLOBOCAN Estimates of Incidence and Mortality Worldwide for 36 Cancers in 185 Countries. CA Cancer J Clin 2021;71(3):209–249. doi: 10.3322/caac.21660
2. Smyth EC, Nilsson M, Grabsch HI, van Grieken NC, Lordick F. Gastric cancer. Lancet 2020;396(10251):635–648. doi: 10.1016/S0140-6736(20)31288-5
3. Japanese Gastric Cancer Treatment Guidelines 2021 (6th edition). Gastric Cancer. Japan2023; p. 1–25.
4. Zhao B, Lv W, Mei D, Luo R, Bao S, Huang B, Lin J. Perineural invasion as a predictive factor for survival outcome in gastric cancer patients: a systematic review and meta-analysis. J Clin Pathol. England2020; p. 544–551.
5. Lordick F, Carneiro F, Cascinu S, Fleitas T, Haustermans K, Piessen G, Vogel A, Smyth EC, clinicalguidelines@esmo.org EGCEa. Gastric cancer: ESMO Clinical Practice Guideline for diagnosis, treatment and follow-up. Ann Oncol 2022;33(10):1005–1020. doi: 10.1016/j.annonc.2022.07.004
6. Ajani JA, D'Amico TA, Bentrem DJ, Chao J, Cooke D, Corvera C, Das P, Enzinger PC, Enzler T, Fanta P, Farjah F, Gerdes H, Gibson MK, Hochwald S, Hofstetter WL, Ilson DH, Keswani RN, Kim S, Kleinberg LR, Klempner SJ, Lacy J, Ly QP, Matkowskyj KA, McNamara M, Mulcahy MF, Outlaw D, Park H, Perry KA, Pimiento J, Poultsides GA, Reznik S, Roses RE, Strong VE, Su S, Wang HL, Wiesner G, Willett CG, Yakoub D, Yoon H, McMillian N, Pluchino LA. Gastric Cancer, Version 2.2022, NCCN Clinical Practice Guidelines in Oncology. J Natl Compr Canc Netw 2022;20(2):167–192. doi: 10.6004/jnccn.2022.0008
7. Zhang M, Mao M, Gong H, Ji D, Fan X, Wang T, Zhu Z. Preoperative Prediction of Perineural Invasion and Survival in Gastric Cancer Using Extracellular Volume Fraction and Dual-Energy CT Quantitative Parameters: A Dual-Center Study. Acad Radiol 2026. doi: 10.1016/j.acra.2026.01.006
8. McCollough CH, Leng S, Yu L, Fletcher JG. Dual- and Multi-Energy CT: Principles, Technical Approaches, and Clinical Applications. Radiology 2015;276(3):637–653. doi: 10.1148/radiol.2015142631
9. Li J, Xu S, Wang Y, Fang M, Ma F, Xu C, Li H. Spectral CT-based nomogram for preoperative prediction of perineural invasion in locally advanced gastric cancer: a prospective study. Eur Radiol. Germany2023; p. 5172–5183.
10. Tomaszewski MR, Gillies RJ. The Biological Meaning of Radiomic Features. Radiology 2021;299(2):E256. doi: 10.1148/radiol.2021219005
11. Stevens JB, Je J, Riley BA, Mowery YM, Brizel DM, Liu JG, Wang C, Lafata KJ. Development and application of a novel tumor habitat analysis technique based on dynamical modeling. Med Phys 2025;52(9):e18032. doi: 10.1002/mp.18032
12. Yao X, Lin J, Hu C, Mao G, Cao Z, Gong W, Wang L, Wang J, Wu S, Ao W. A Novel CT Habitat Radiomics Approach for HER2 Status Prediction in Gastric Cancer. Acad Radiol 2026. doi:

10.1016/j.acra.2026.02.039

13. Hoover G, Gilbert S, Curley O, Obellianne C, Lin MT, Hixson W, Pierce TW, Andrews JF, Alexeyev MF, Ding Y, Bu P, Behbod F, Medina D, Chang JT, Ayala G, Grelet S. Nerve-to-cancer transfer of mitochondria during cancer metastasis. Nature. England2025; p. 252–262.
14. Deborde S, Wong RJ. How Schwann cells facilitate cancer progression in nerves. Cell Mol Life Sci. Switzerland2017; p. 4405–4420.
15. Wang H, Huang G, Zhao Z, Cheng L, Juncker-Jensen A, Nagy ML, Lu X, Zhang X, Chen DZ. CCF-GNN: A Unified Model Aggregating Appearance, Microenvironment, and Topology for Pathology Image Classification. IEEE Trans Med Imaging 2023;42(11):3179–3193. doi: 10.1109/TMI.2023.3249343
16. Gogoshin G, Rodin AS. Graph Neural Networks in Cancer and Oncology Research: Emerging and Future Trends. Cancers (Basel). Switzerland2023.
17. Chatterjee P, Siddiqui S, Kareem RSA, Rao SR. Multi-Modal Graph Neural Networks for Colposcopy Data Classification and Visualization. Cancers (Basel). Switzerland2025.
18. Elhalawani H, Mak R. Are Artificial Intelligence Challenges Becoming Radiology's New "Bee's Knees"? Radiol Artif Intell 2021;3(3):e210056. doi: 10.1148/ryai.2021210056
19. Ma X, Ji P, Zheng J, Cai S, Xu K, Sun Y, Liu D. Neuro-tumor interactions in peripheral tumors. Cancer Metastasis Rev 2026;45(2). doi: 10.1007/s10555-026-10321-6
20. Yang YC, Wu JJ, Shi F, Ren QG, Jiang QJ, Guan S, Tang XQ, Meng XS. Sub-regional Radiomics Analysis for Predicting Metastasis Risk in Clear Cell Renal Cell Carcinoma: A Multicenter Retrospective Study. Acad Radiol 2025;32(1):237–249. doi: 10.1016/j.acra.2024.08.006
21. Su Y, Zhao H, Lyu Z, Xu P, Zhang Z, Zhang H, Wang M, Tian L, Fu P. Quantification of Intratumoral Heterogeneity Based on Habitat Analysis for Preoperative Assessment of Lymphovascular Invasion in Colorectal Cancer. Acad Radiol 2025;32(8):4532–4543. doi: 10.1016/j.acra.2025.03.014
22. Jiang P, Zheng L, Yang Y, Mo D. Establishment and validation of a prediction model for gastric cancer with perineural invasion based on preoperative inflammatory markers. Transl Cancer Res. China2024; p. 5381–5394.

Figures

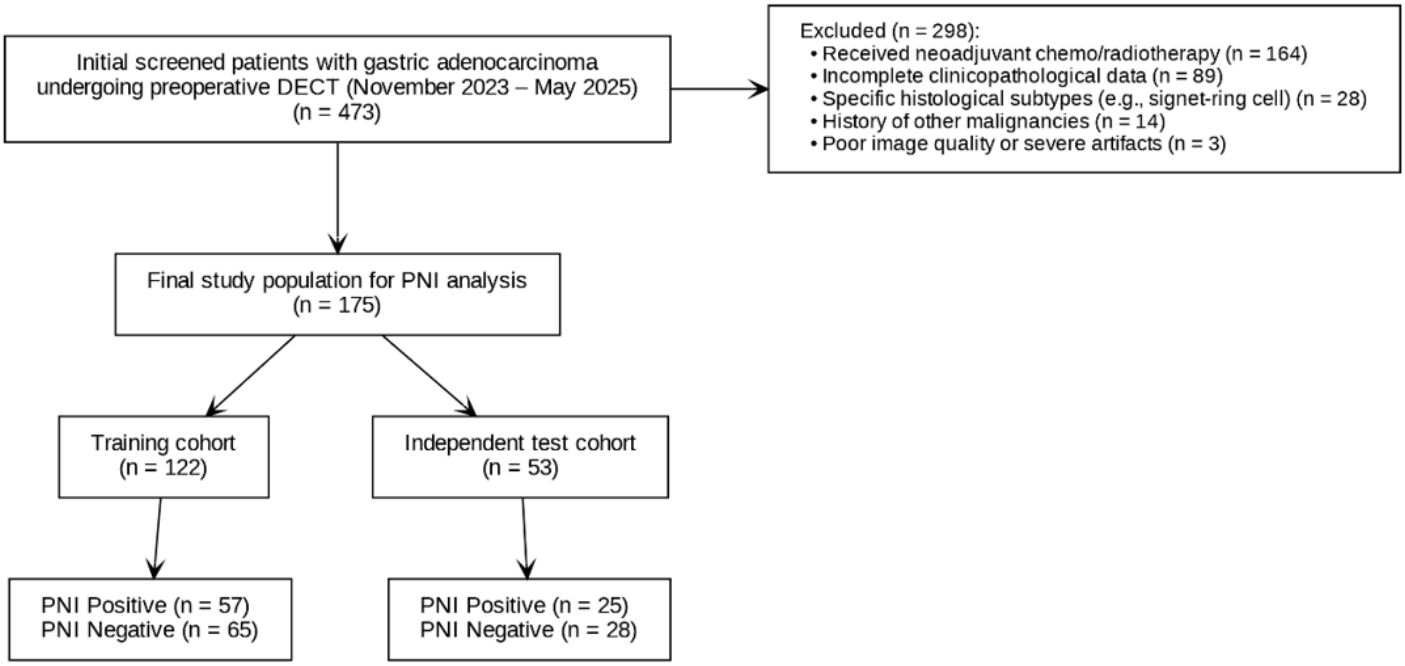


Figure 1

Flowchart of patient selection and data partitioning.

Note.— Flowchart illustrates the recruitment process and exclusion logic for the study population. Of the 473 initially screened patients with gastric adenocarcinoma, 298 were excluded based on pre-specified criteria, most notably the receipt of neoadjuvant therapy (*n* = 164) and incomplete clinicopathological data (*n* = 89). The final cohort of 175 patients was stratified by PNI status and randomly assigned to the training cohort (*n* = 122) for model development and the independent test cohort (*n* = 53) for performance validation. PNI = perineural invasion, DECT = dual-energy CT.

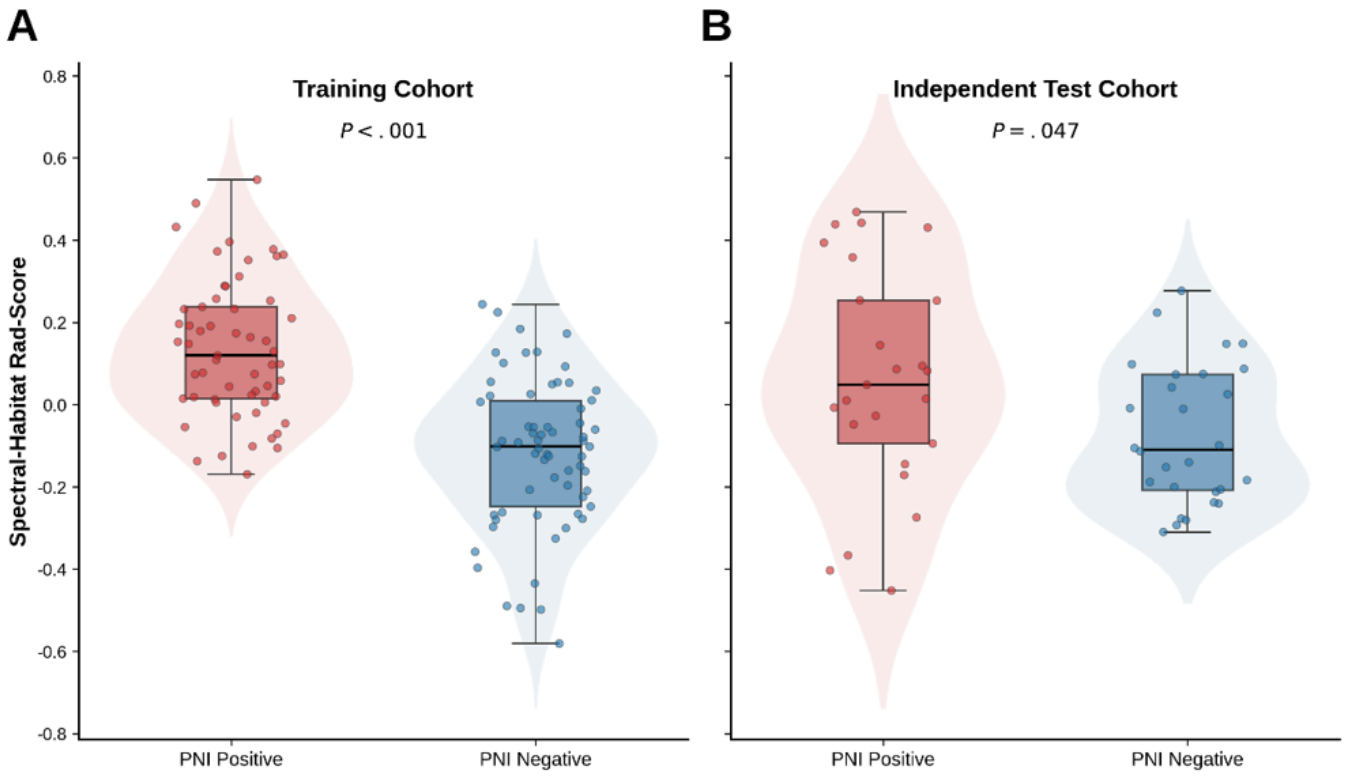


Figure 2

Distribution of the Spectral-Habitat Rad-scores in the training and independent test cohorts.

Note.— Dual-violin and box plots illustrate the scores for patients with (red) and without (blue) pathologically confirmed perineural invasion (PNI) in the **(A)** training cohort (*n* = 122) and **(B)** independent test cohort (*n* = 53). Horizontal lines within the boxes indicate medians; boxes indicate the interquartile range; and whiskers indicate the range of data excluding outliers. Shaded areas represent the kernel density estimation of the score distribution. Individual data points are shown as jittered dots. *P* values were derived from the Mann-Whitney U test. The discriminatory power of the signature was successfully validated in the independent test cohort (***P* = .047**).

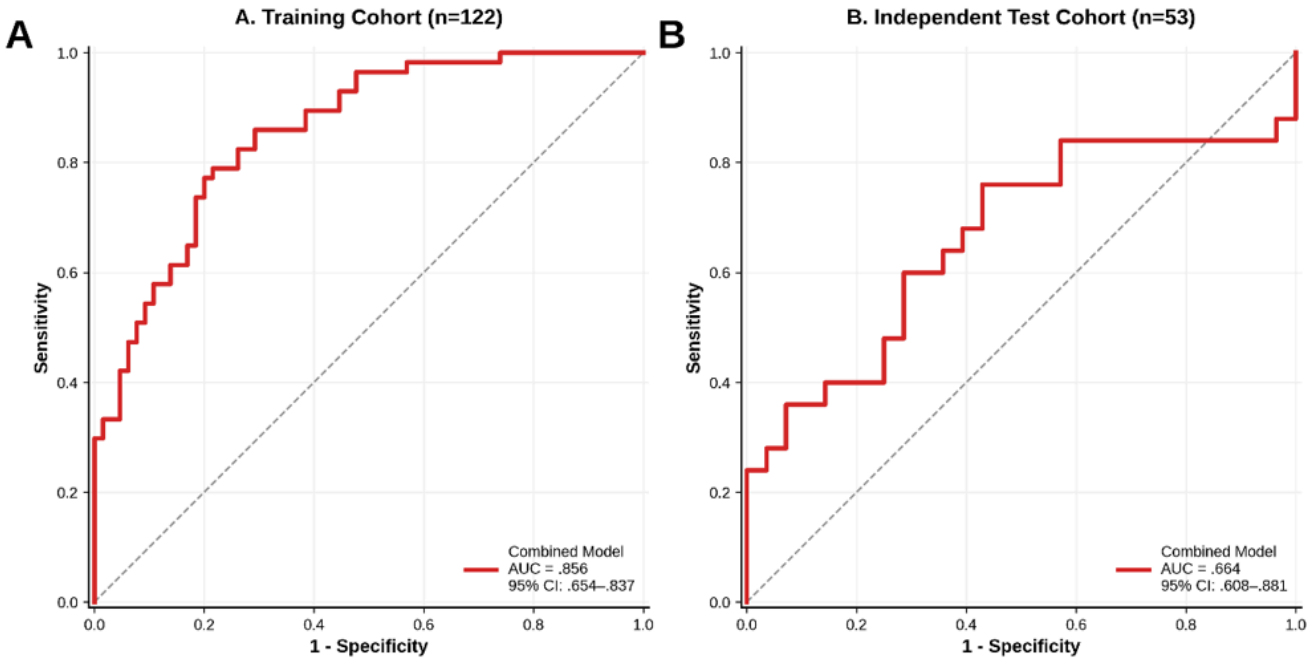


Figure 3

Receiver operating characteristic (ROC) curves for the prediction of perineural invasion.

Note.— Curves illustrate the diagnostic performance of the integrated model in the **(A)** training cohort and **(B)** independent test cohort. The training cohort yields an AUC of .748 (95% CI: .654, .837), and the independent test cohort yields a validated AUC of .753 (95% CI: .608, .881). The proximity of the AUC values between cohorts indicates excellent model generalizability and a lack of overfitting. The integrated model (red solid line) demonstrated significantly improved performance compared with the habitat-only radiomics baseline (blue dashed line) in the test set (*P*=.011, DeLong test).

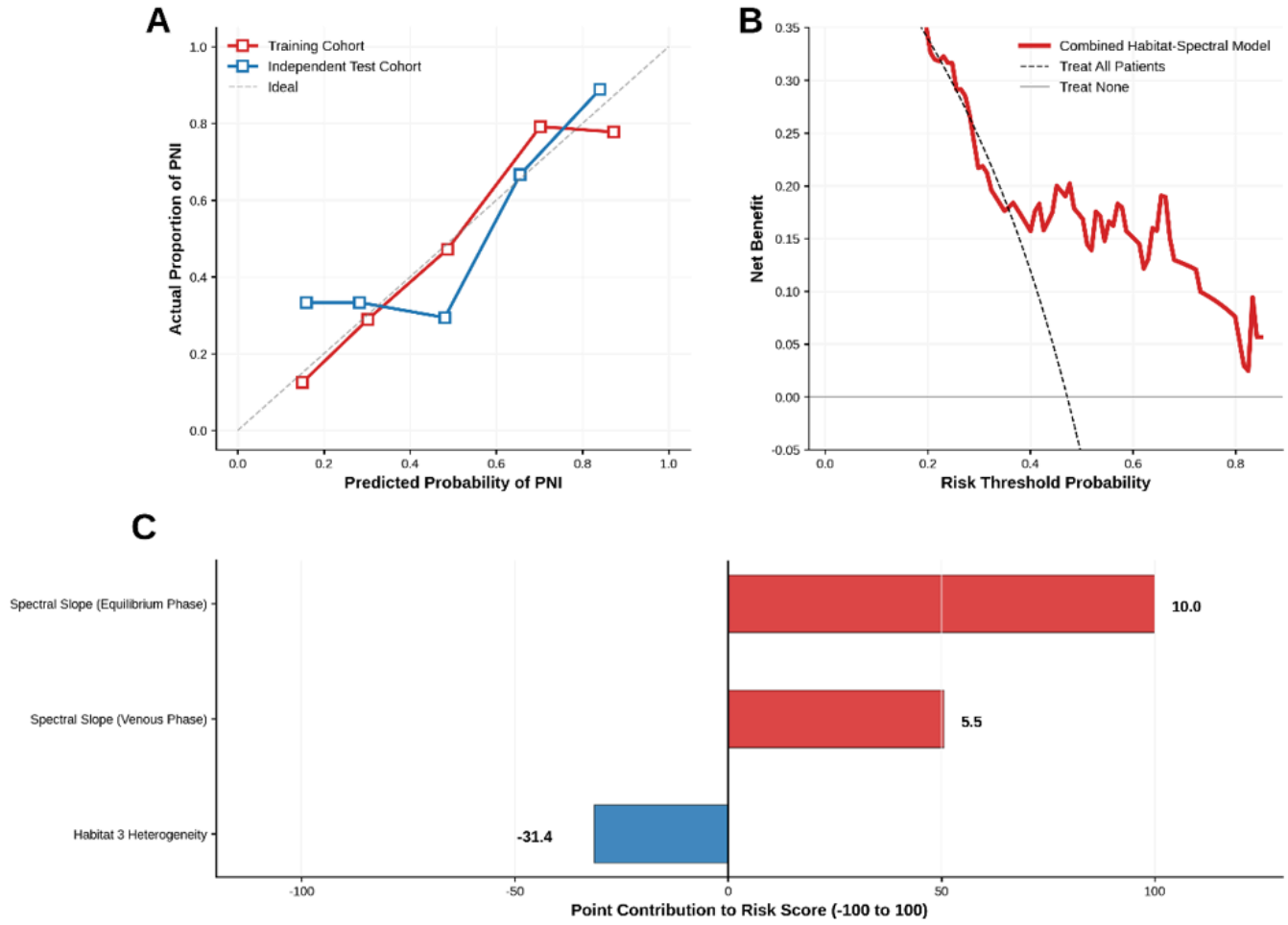


Figure 4

Model calibration, clinical utility, and individualized risk estimation.

Note.— (A) Calibration curves for the training and independent test cohorts. The curves align closely with the 45° diagonal line, reflecting high predictive reliability.

(B) Decision curve analysis demonstrating the net clinical benefit of the model (red line) compared to baseline strategies.

(C) Point scoring system based on standardized coefficients. Points represent the relative contribution of each feature to the final risk estimation.

Supplementary Files

This is a list of supplementary files associated with this preprint. Click to download.

- SupplementaryFigures.docx